Observer-based state-space current control for a three-phase grid-connected converter equipped with an LCL filter — Source link ↗

Jarno Kukkola, Marko Hinkkanen

Institutions: Aalto University

Related papers:

- Regions of Active Damping Control for LCL Filters

- Full-State Feedback Equivalent Controller for Active Damping in LCL -Filtered Grid-Connected Inverters Using a Reduced Number of Sensors

- PI State Space Current Control of Grid-Connected PWM Converters With LCL Filters

- Digital Current Control of a Voltage Source Converter With Active Damping of LCL Resonance

- Overview of Control and Grid Synchronization for Distributed Power Generation Systems

Share this paper: 🅕 🅣 🔗 ✉

Author(s): Kukkola, Jarno & Hinkkanen, Marko

Title: Observer-Based State-Space Current Control for a Three-Phase Grid-Connected Converter Equipped With an LCL Filter

Year: 2014

Version: Post print

Please cite the original version:

Observer-Based State-Space Current Control for a Three-Phase Grid-Connected Converter Equipped With an LCL Filter

Jarno Kukkola and Marko Hinkkanen, *Senior Member, IEEE*

Abstract—**This paper presents a state-space current control method for active damping of the resonance frequency of the LCL filter and setting the dominant dynamics of the converter current through direct pole placement. A state observer is used, whereupon additional sensors are not needed in comparison with the conventional L filter design. The relationship between the system delay and instability caused by the resonance phenomenon is considered. Nyquist diagrams are used to examine the parameter sensitivity of the proposed method. The method is validated with simulations and experiments.**

Index Terms—**Delay, LCL filter, Nyquist diagram, parameter sensitivity, phase-lead compensator, state-space current control.**

I. Introduction

LCL filters for three-phase, voltage-source, grid-connected converters have been in great interest during the past few years. The LCL filter offers better attenuation of switching harmonics above the resonance frequency of the filter in comparison with the traditional L filter with an equal inductance to the inductance of the LCL filter. A disadvantage of the LCL filters is the resonant behavior.

The resonance of the LCL filter can be damped actively [1] or passively at the expense of losses [2]. Numerous different active resonance damping methods have been proposed in the literature: 1) filtering the output signal of a proportional integral (PI) current controller [3], [4]; 2) additional feedback of the capacitor voltage or capacitor current [1], [5], [6]; 3) adding a virtual resistor with an additional control algorithm [7], [8]; 4) passivity-based control design [9]; and 5) state-feedback and predictive methods [10]–[18]. Some of these active damping methods require extra sensors in comparison with the conventional L filter design (where the converter current and grid voltage are measured). Additional sensors are needed, for instance, in the active damping methods based on capacitor-current feedback [5] and state feedback [10], [13], while the capacitor voltage measurements can be utilized for the synchronization in the capacitor-voltage-based active damping method [1]. The extra sensors increase costs and decrease reliability. The number of measurements can be reduced by state estimation [6], [8], [11], [14]–[19]. In addition to state estimation, the grid-voltage sensors are eliminated in [6], [8], [15], [17] and grid-voltage disturbances are estimated in [15], [19].

J. Kukkola and M. Hinkkanen are with Aalto University School of Electrical Engineering, P.O. Box 13000, FI-00076 Aalto, Espoo, Finland (e-mail: jarno.kukkola@aalto.fi; marko.hinkkanen@aalto.fi).

State-space control is attractive in the case of the LCL filter because it enables setting the dominant dynamics and resonant dynamics (i.e. resonance damping) using pole placement. This can be done directly by selecting the desired pole locations [13], [14], using dead-beat control [10], optimizing some cost function as in linear quadratic (LQ) control [15], [16], or with Bessel functions [11]. A natural way to the pole placement is the direct pole placement based on the open-loop poles and the desired dynamics of the closed-loop system, as in [13]. With this approach, the controller gains can be analytically expressed with the parameters of the system and dynamic performance specifications, but this may lead to long expressions, if the discrete-time domain is used [13].

The transport delay, caused by calculation of control quantities and pulse-width modulation process, is an important issue in current control of the LCL-filter system. The delay induces stability problems in different frequency regions in the case of grid-current feedback and in the case of converter-current feedback [4], [20]. In other words, the system equipped with grid-current feedback has a tendency to become unstable if the resonance frequency of the filter is low (in comparison with the sampling frequency), while the system with converter-current feedback has a tendency to become unstable if the resonance frequency is high. Thus, an important factor is the ratio of the resonance frequency to the delay frequency, which is closely related to the sampling frequency. This ratio has been used to give limits for the stable operation of pure PI control [20], [21].

In this paper, a complete grid-voltage oriented state-space current control method for a three-phase, voltage-source, grid-connected converter with an LCL filter is designed based on the continuous switching-cycle-averaged model of the converter. Converter-current feedback is selected because then the current sensors can be integrated inside the converter, protection of the converter is simple, and the LCL filter can be installed as a separate module. Furthermore, a full-order observer is used, whereupon additional sensors are not needed in comparison with the conventional L filter design. Nyquist diagrams are used to examine the parameter sensitivity of the proposed design. Finally, the control method is validated with simulations and experiments. The main contributions of this paper are: 1) the direct pole-placement strategy in the continuous-time domain giving relatively simple expressions for the gains of the state-space controller and the full-order observer in terms of model parameters and the desired dynamics; 2) the compensation of the cross-coupling with the

direct pole-placement strategy contrary to [13]; 3) the ratio of the resonance frequency and the delay frequency is examined analytically in the case of converter-current feedback; 4) an additional phase-lead compensator, as a modular block, is used to compensate the destabilizing effect of the system delay.

II. SYSTEM MODEL

A grid-connected converter with an LCL filter is shown in Fig. 1(a) and the block diagram of the current control scheme is shown in Fig. 1(b). The dc-link voltage u_{d}, line-to-line grid voltages u_{gab} and u_{gbc}, and converter-side currents i_{ca}, i_{cb}, i_{cc} are measured for control. Complex-valued space vectors in synchronous coordinates are used, e.g., the grid-voltage vector is $\boldsymbol{u}_{\mathrm{g}} = u_{\mathrm{gd}} + \mathrm{j}u_{\mathrm{gq}}$. Complex-valued quantities, matrices, and vectors are marked with boldface.

The current controller and the state observer operate in grid-voltage-oriented synchronous coordinates, where $\boldsymbol{u}_{\mathrm{g}} = u_{\mathrm{gd}} + \mathrm{j}0$. A phase-locked loop (PLL) based on synchronous reference frame transformation [22], [23] is used to detect the grid-voltage angle $\vartheta_{\mathrm{g}} = \int \omega_{\mathrm{g}}\mathrm{d}t$, where ω_{g} is the grid angular frequency. The gate signals for the switches are generated using space-vector pulse-width modulation (SVPWM).

The state vector is selected as $\mathbf{x} = [\boldsymbol{i}_{\mathrm{c}} \; \boldsymbol{u}_{\mathrm{f}} \; \boldsymbol{i}_{\mathrm{g}}]^{\mathrm{T}}$, where $\boldsymbol{u}_{\mathrm{f}}$ is the voltage across the filter capacitor C_{f}, and $\boldsymbol{i}_{\mathrm{c}}$ and $\boldsymbol{i}_{\mathrm{g}}$ are the converter and grid currents, respectively. In synchronous coordinates rotating at the grid angular frequency ω_{g}, the dynamics of the converter current $\boldsymbol{i}_{\mathrm{c}}$ can be represented in the state-space form

$$
\frac{\mathrm{d}\mathbf{x}}{\mathrm{d}t} = \underbrace{\begin{bmatrix} -\mathrm{j}\omega_{\mathrm{g}} & -\frac{1}{L_{\mathrm{fc}}} & 0 \\ \frac{1}{C_{\mathrm{f}}} & -\mathrm{j}\omega_{\mathrm{g}} & -\frac{1}{C_{\mathrm{f}}} \\ 0 & \frac{1}{L_{\mathrm{fg}}} & -\mathrm{j}\omega_{\mathrm{g}} \end{bmatrix}}_{\mathbf{A}} \mathbf{x} + \underbrace{\begin{bmatrix} \frac{1}{L_{\mathrm{fc}}} \\ 0 \\ 0 \end{bmatrix}}_{\mathbf{B}_{\mathrm{c}}} \boldsymbol{u}_{\mathrm{c}} + \underbrace{\begin{bmatrix} 0 \\ 0 \\ -\frac{1}{L_{\mathrm{fg}}} \end{bmatrix}}_{\mathbf{B}_{\mathrm{g}}} \boldsymbol{u}_{\mathrm{g}}
$$

$$
\boldsymbol{i}_{\mathrm{c}} = \underbrace{\begin{bmatrix} 1 & 0 & 0 \end{bmatrix}}_{\mathbf{C}_{\mathrm{c}}} \mathbf{x}
\tag{1}
$$

where $\boldsymbol{u}_{\mathrm{c}}$ is the converter output voltage. Losses of the filter components (L_{fc}, C_{f}, L_{fg}) are neglected, representing the worst-case situation for the resonance of the LCL filter.

The transfer function (input admittance) from the converter voltage to the converter current can be calculated from (1):

$$
\boldsymbol{Y}(s) = \frac{\boldsymbol{i}_{\mathrm{c}}(s)}{\boldsymbol{u}_{\mathrm{c}}(s)} = \mathbf{C}_{\mathrm{c}}(s\mathbf{I} - \mathbf{A})^{-1}\mathbf{B}_{\mathrm{c}}
$$
$$
= \frac{1}{L_{\mathrm{fc}}} \frac{(s + \mathrm{j}\omega_{\mathrm{g}})^2 + (\omega_{\mathrm{z}}^{\mathrm{s}})^2}{(s + \mathrm{j}\omega_{\mathrm{g}})[(s + \mathrm{j}\omega_{\mathrm{g}})^2 + (\omega_{\mathrm{p}}^{\mathrm{s}})^2]}
\tag{2}
$$

where

$$
\omega_{\mathrm{p}}^{\mathrm{s}} = \sqrt{\frac{L_{\mathrm{fc}} + L_{\mathrm{fg}}}{L_{\mathrm{fc}} L_{\mathrm{fg}} C_{\mathrm{f}}}} \qquad \omega_{\mathrm{z}}^{\mathrm{s}} = \sqrt{\frac{1}{L_{\mathrm{fg}} C_{\mathrm{f}}}}
\tag{3}
$$

are the resonance frequency and the anti-resonance frequency, respectively, in stationary coordinates. As can be seen from (2), the resonance frequencies in synchronous coordinates are shifted by ω_{g} to lower frequencies due to the coordinate transformation, e.g., the resonance frequency in synchronous coordinates is $\omega_{\mathrm{p}} = \omega_{\mathrm{p}}^{\mathrm{s}} - \omega_{\mathrm{g}}$. The other transfer functions of the open-loop system are obtained similarly: for the capacitor

voltage $\boldsymbol{u}_{\mathrm{f}}$, the output vector is $\mathbf{C}_{\mathrm{u}} = [0 \; 1 \; 0]$, and for the grid current $\boldsymbol{i}_{\mathrm{g}}$, the output vector is $\mathbf{C}_{\mathrm{g}} = [0 \; 0 \; 1]$.

In the following analysis, SVPWM is assumed to operate in the linear region. The system delay of $T_{\mathrm{d}} = 3T_{\mathrm{s}}/2$ is considered, where T_{s} is the sampling period. The angle error caused by the delay is compensated for in the coordinate transformation. Hence, the converter output voltage $\boldsymbol{u}_{\mathrm{c}} = u_{\mathrm{cd}} + \mathrm{j}u_{\mathrm{cq}}$ is modeled as

$$
\boldsymbol{u}_{\mathrm{c}}(t) = \boldsymbol{u}_{\mathrm{c,ref}}(t - T_{\mathrm{d}})
\tag{4}
$$

where the reference voltage $\boldsymbol{u}_{\mathrm{c,ref}}$ is the output of the current controller.

III. CURRENT CONTROL DESIGN

The current control structure is shown in Fig. 1(b). The voltage reference $\boldsymbol{u}_{\mathrm{c,ref}}$ for the modulator is produced by a state-space controller together with a phase-lead compensator. A full-order state observer is used to produce the estimates $\hat{\boldsymbol{u}}_{\mathrm{f}}$ and $\hat{\boldsymbol{i}}_{\mathrm{g}}$ for the capacitor voltage and the grid current, respectively. The converter current estimate $\hat{\boldsymbol{i}}_{\mathrm{c}}$ is also available but the measured current $\boldsymbol{i}_{\mathrm{c}}$ is used in feedback instead. However, if the measured current is noisy, it may be advantageous to use the estimated current in feedback due to natural filtering behavior of the observer. Furthermore, the state-space controller could be augmented with a resonant controller in order to improve performance in distorted conditions [13], [24].

The current controller design process can be separated into three steps: 1) the state-space controller is designed by assuming that all the states are known and the delay is neglected; 2) the observer is designed by selecting the dynamics for the estimation error; 3) the ratio of the system delay frequency and the resonance frequency is examined and the phase-lead compensator is designed to compensate the phase lag of the delay, if needed.

A. State-Space Controller

The converter current is controlled with a state-space controller that produces the control voltage

$$
\boldsymbol{u}_{\mathrm{c,ref}}' = \boldsymbol{k}_{\mathrm{T}}\boldsymbol{i}_{\mathrm{c,ref}} + \boldsymbol{k}_{\mathrm{I}}\boldsymbol{x}_{\mathrm{I}} - \mathbf{K}\mathbf{x}
\tag{5}
$$

where $\boldsymbol{i}_{\mathrm{c,ref}}$ is the reference, $\boldsymbol{k}_{\mathrm{T}}$ is the feed-forward gain, $\boldsymbol{k}_{\mathrm{I}}$ is the gain of the integral state $\boldsymbol{x}_{\mathrm{I}} = \int (\boldsymbol{i}_{\mathrm{c,ref}} - \boldsymbol{i}_{\mathrm{c}})\mathrm{d}t$, and $\mathbf{K} = [\boldsymbol{k}_1 \; \boldsymbol{k}_2 \; \boldsymbol{k}_3]$ is the feedback gain vector. With the assumptions $\mathbf{x} = [\boldsymbol{i}_{\mathrm{c}} \; \boldsymbol{u}_{\mathrm{f}} \; \boldsymbol{i}_{\mathrm{g}}]^{\mathrm{T}}$ is known and $\boldsymbol{u}_{\mathrm{c,ref}}' = \boldsymbol{u}_{\mathrm{c}}$, the closed-loop dynamics are obtained from (1) and (5),

$$
\begin{bmatrix} \dot{\mathbf{x}} \\ \dot{\boldsymbol{x}}_{\mathrm{I}} \end{bmatrix} = \underbrace{\begin{bmatrix} \mathbf{A} - \mathbf{B}_{\mathrm{c}}\mathbf{K} & \mathbf{B}_{\mathrm{c}}\boldsymbol{k}_{\mathrm{I}} \\ -\mathbf{C}_{\mathrm{c}} & 0 \end{bmatrix}}_{\tilde{\mathbf{A}}} \begin{bmatrix} \mathbf{x} \\ \boldsymbol{x}_{\mathrm{I}} \end{bmatrix} + \underbrace{\begin{bmatrix} \mathbf{B}_{\mathrm{c}}\boldsymbol{k}_{\mathrm{T}} \\ 1 \end{bmatrix}}_{\tilde{\mathbf{B}}} \boldsymbol{i}_{\mathrm{c,ref}}
$$
$$
+ \begin{bmatrix} \mathbf{B}_{\mathrm{g}} \\ 0 \end{bmatrix} \boldsymbol{u}_{\mathrm{g}}
\tag{6}
$$
$$
\boldsymbol{i}_{\mathrm{c}} = \underbrace{\begin{bmatrix} \mathbf{C}_{\mathrm{c}} & 0 \end{bmatrix}}_{\tilde{\mathbf{C}}} \begin{bmatrix} \mathbf{x} \\ \boldsymbol{x}_{\mathrm{I}} \end{bmatrix}
$$

where $\tilde{\mathbf{A}}$ is the system matrix, $\tilde{\mathbf{B}}$ the control matrix, and $\tilde{\mathbf{C}}$ the output vector of the closed-loop system. The influence of

Fig. 1.   (a) Grid-connected converter with an LCL filter. (b) Current control structure. The angle $\omega_g T_d$ due to the delay is compensated for in the dq→abc transformation and the anti-windup is implemented (not explicitly shown in the figure).

the grid voltage $\boldsymbol{u}_g$ is considered as a disturbance. From (6), the transfer function of the closed-loop system is

$$G_{cl}(s) = \frac{\boldsymbol{i}_c(s)}{\boldsymbol{i}_{c,ref}(s)} = \tilde{\mathbf{C}}(s\mathbf{I} - \tilde{\mathbf{A}})^{-1}\tilde{\mathbf{B}}. \tag{7}$$

The closed-loop current control dynamics are set through direct pole placement in synchronous coordinates. If the closed-loop poles are selected as

$$\underbrace{(s^2 + 2\zeta_1\omega_1 s + \omega_1^2)}_{\text{Dominant dynamics}}\underbrace{(s^2 + 2\zeta_2\omega_2 s + \omega_2^2)}_{\text{Resonant dynamics}}, \tag{8}$$

the controller gains can be calculated by equalizing the characteristic polynomial of (7) and (8):

$$\boldsymbol{k}_1 = 2L_{fc}(\zeta_1\omega_1 + \zeta_2\omega_2) - 3j\omega_g L_{fc} \tag{9a}$$

$$\boldsymbol{k}_2 = L_{fc}C_f\Big(\omega_1^2 + \omega_2^2 + 4\zeta_1\omega_1\zeta_2\omega_2 + 3\omega_g^2 - \frac{2j\omega_g}{L_{fc}}\boldsymbol{k}_1$$
$$- \frac{\boldsymbol{k}_I}{L_{fc}} - \frac{1}{L_{fg}C_f}\Big) - 1 \tag{9b}$$

$$\boldsymbol{k}_3 = (\omega_g^2 L_{fg}C_f - 1)\boldsymbol{k}_1 + L_{fc}L_{fg}C_f\Big[2\zeta_1\omega_1\omega_2^2 + 2\zeta_2\omega_2\omega_1^2$$
$$+ j\omega_g\Big(\omega_g^2 - \frac{1}{L_{fg}C_f} - \frac{\boldsymbol{k}_2+1}{L_{fc}C_f} - \frac{2\boldsymbol{k}_I}{L_{fc}}\Big)\Big] \tag{9c}$$

$$\boldsymbol{k}_I = \frac{\omega_1^2\omega_2^2 L_{fc}L_{fg}C_f}{1 - \omega_g^2 L_{fg}C_f}. \tag{9d}$$

Dominant behavior of the closed-loop system is set with the dominant part of (8). The natural frequency of the dominant dynamics is ω_1 with the damping factor ζ_1. The damping is selected to a high value $\zeta_1 = 0.7\ldots1$ to prevent large overshoots. If the dominant pole pair is damped critically, i.e. $\zeta_1 = 1$, there is a double pole at the frequency ω_1 of which the pole from the integrator can be compensated with the feedforward gain

$$\boldsymbol{k}_T = \frac{\boldsymbol{k}_I}{\omega_1}. \tag{10}$$

It is to be noted that the proposed pole placement leads to real $\boldsymbol{k}_I$ and $\boldsymbol{k}_T$, cf. (9d).

With the resonant part of (8), the resonance of the LCL filter can be damped and the resonance frequency can be moved, if desired. A good basis to select these resonant dynamics is to let the resonance frequency stay close to its natural value, i.e. $\omega_2 \approx \omega_p$. Damping of the resonant pole pair is set to a low value $\zeta_2 = 0.05\ldots0.3$ in order to keep the control effort reasonable but to provide enough resonance damping. Furthermore, nonzero delay T_d limits the maximum value of ζ_2 (cf. Section III-E). In practice, the losses of the filter, particularly in the vicinity of the resonance frequency, also increase damping.

The cross-coupling between the d and q components of the converter current is compensated automatically with the pole placement in (8). Alternatively, to decrease the control effort, the cross-coupling could be left in the resonant dynamics if the resonant part of (8) were selected as

$$(s + j\omega_g)^2 + 2\zeta_2\omega_2(s + j\omega_g) + \omega_2^2. \tag{11}$$

B. State Observer

Because the converter current $\boldsymbol{i}_c$ and the grid voltage $\boldsymbol{u}_g$ are measured and the converter voltage $\boldsymbol{u}_c$ is internally known according to (4), the rest of the states for the controller can be estimated using a full-order observer [25]

$$\frac{d\hat{\mathbf{x}}}{dt} = \mathbf{A}\hat{\mathbf{x}} + \mathbf{B}_c\boldsymbol{u}_c + \mathbf{B}_g\boldsymbol{u}_g + \mathbf{L}(\boldsymbol{i}_c - \hat{\boldsymbol{i}}_c) \tag{12a}$$

$$\hat{\boldsymbol{i}}_c = \mathbf{C}_c\hat{\mathbf{x}} \tag{12b}$$

where $\mathbf{L} = [l_1\ l_2\ l_3]^T$ is the observer gain vector. With (1) and (12), the dynamics of the estimation error $\tilde{\mathbf{x}} = \mathbf{x} - \hat{\mathbf{x}}$ are $d\tilde{\mathbf{x}}/dt = (\mathbf{A} - \mathbf{LC}_c)\tilde{\mathbf{x}}$. If the characteristic polynomial of the observer dynamics is selected as

$$\det(s\mathbf{I} - \mathbf{A} + \mathbf{LC}_c) = (s + \alpha_{o1})(s^2 + 2\zeta_{o2}\omega_{o2}s + \omega_{o2}^2),$$

where α_{o1} determines the first-order pole, and ζ_{o2} and ω_{o2} the second-order pole pair, the observer gains can be calculated

$$l_1 = \alpha_{o1} + 2\zeta_{o2}\omega_{o2} - 3j\omega_g \quad (13a)$$

$$l_2 = -L_{fc}\left(2\alpha_{o1}\zeta_{o2}\omega_{o2} + \omega_{o2}^2 + 3\omega_g^2 - \frac{L_{fc} + L_{fg}}{L_{fc}L_{fg}C_f} - 2j\omega_g l_1\right) \quad (13b)$$

$$l_3 = \alpha_{o1}\omega_{o2}^2 C_f L_{fc} + j\omega_g\left(\omega_g^2 C_f L_{fc} - \frac{L_{fc}}{L_{fg}} - 1\right)$$
$$+ \left(\omega_g^2 C_f L_{fc} - \frac{L_{fc}}{L_{fg}}\right)l_1 + j\omega_g C_f l_2. \quad (13c)$$

This selection removes the cross-coupling in the observer dynamics. Alternatively, the cross-coupling could be left in the higher-order dynamics in the similar manner as in (11).

The poles of the closed-loop system consist of the union of the controller poles and the observer poles [25]. A rule of thumb is to select the observer poles to be $2\ldots6$ times faster than the poles of the state-space controller. Then, the observer dynamics do not limit the bandwidth determined by the controller. However, the discrete-time implementation with the Nyquist frequency of $\omega_N = \pi/T_s$ gives the highest limit for the observer poles.

C. System Delay

The transfer function of the delay, corresponding to (4), is

$$G_d(s) = e^{-sT_d} \quad (14)$$

of which amplitude is always unity and the phase is linearly decreasing, $\angle G_d(j\omega) = -\omega T_d$. From the current controller point of view, the delay $G_d(s)$ and the LCL filter can be considered as one open-loop system $i_c(s)/u_{c,ref}(s) = G_d(s)Y(s)$, as described in [20]. Then, the angle of the open-loop frequency response at the resonance frequency ω_p (in synchronous coordinates) can be expressed as

$$\angle[G_d(j\omega_p)Y(j\omega_p)] = -\omega_p T_d - \pi/2.$$

Further, if the delay is described with the delay angular frequency $\omega_d = 2\pi/T_d$, the phase margin of the open-loop system at the resonance frequency can be calculated

$$\text{PM}_R = \pi - \omega_p\frac{2\pi}{\omega_d} - \frac{\pi}{2} = 2\pi\left(\frac{1}{4} - \frac{\omega_p}{\omega_d}\right). \quad (15)$$

This equation shows that the system with a unity controller is unstable (the phase margin is negative at the resonance frequency) if $\omega_d < 4\omega_p$. Fig. 2 shows the open-loop frequency responses of $G_d(s)Y(s)$ with different ratios of the delay frequency to the resonance frequency. With long delays (low switching frequencies), the phase of the open-loop system is turning below $-180°$ when the gain is above unity (the gain is infinity in the worst-case scenario). Thus, some phase compensation is needed if the delay frequency is close to the resonance frequency, e.g. the phase-lead compensator or the Smith predictor. The phase-lead compensator is selected for the sake of simplicity.
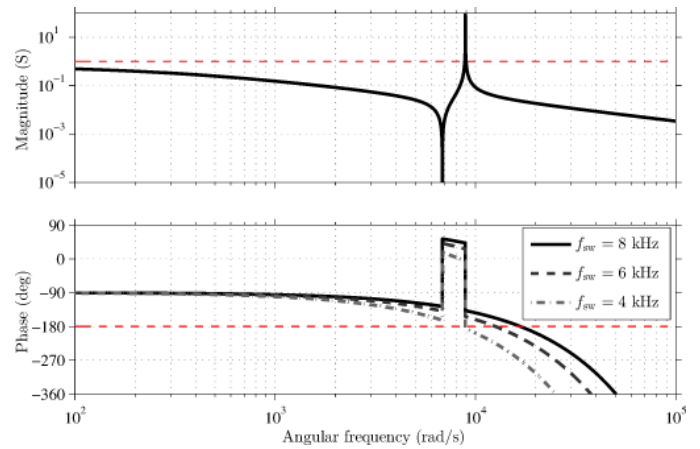

Fig. 2.   Influence of the system delay in the open-loop transfer function $G_d(s)Y(s)$: $L_{fc} = 2.94$ mH, $L_{fg} = 1.96$ mH, and $C_f = 10$ μF ($\omega_p^s \approx$ 9220 rad/s). The delay is $T_d = (3/2)T_s = 3/(4f_{sw})$ when two samples per switching period are obtained. The limits of 1 and $-180°$ are marked with red dashed lines.

D. Phase-Lead Compensator

Adding a phase lead with the phase-lead compensator in the vicinity of the resonance frequency is straightforward. The transfer function of the phase-lead compensator is

$$G_L(s) = A_L\frac{1 + \frac{s}{\omega_L}}{1 + \frac{s}{k_L\omega_L}} \quad (16)$$

where A_L is the gain and $k_L > 1$ is the ratio of the pole $k_L\omega_L$ and the zero ω_L of the filter. The maximum phase lead is provided at the frequency of

$$\omega_m = \sqrt{k_L}\omega_L. \quad (17)$$

The relation between the maximum phase lead ϕ_m and k_L is [25]

$$k_L = \frac{1 + \sin\phi_m}{1 - \sin\phi_m}. \quad (18)$$

The phase-lead compensator is designed based on the open-loop phase margin at the resonance frequency (15) by the following steps:

1) The maximum phase lead is produced at the resonance frequency, i.e. $\omega_m = \omega_p = \omega_p^s - \omega_g$.
2) The maximum phase lead ϕ_m is calculated from the difference of the desired phase margin (e.g. $40°$) with the unity controller and the open-loop margin (15).
3) The parameter k_L is calculated from (18) and ω_L from (17).
4) The parameter A_L is selected to give unity gain for $G_L(s)$ at the Nyquist frequency $\omega_N = \pi/T_s$. Hence, the gain at the resonance frequency is not increased (since $\omega_p < \omega_N$) and measurement noise is not amplified. Unity gain at the infinity, i.e. $A_L = 1/k_L$, gives a good approximation for small phase leads.

The maximum phase lead for the compensator in (16) is $\pi/2$. However, increasing the amount of the phase lead, either noise sensitivity is increased or disturbance rejection of current control is decreased depending on the selection of the gain A_L.

E. Parameter Sensitivity

The grid impedance was neglected in the gain calculation of the state-space controller. The variation of the grid impedance effectively changes the value of the inductance L_{fg}. Here, the effect of varying inductance on current control is examined with Nyquist diagrams of the loop-transfer function $\boldsymbol{H}(s)$ of the whole feedback loop.

When the current reference is set to zero, i.e. $\boldsymbol{i}_{\mathrm{c,ref}} = 0$, and the grid voltage as a disturbance is neglected, the control voltage $\boldsymbol{u}_{\mathrm{c,ref}}$ produced by the controller, observer, and phase-lead compensator is

$$\boldsymbol{u}_{\mathrm{c,ref}}(s) = -G_{\mathrm{L}}(s)\Big\{\big[\boldsymbol{k}_2\boldsymbol{G}_{21}(s) + \boldsymbol{k}_3\boldsymbol{G}_{31}(s)\big]\boldsymbol{u}_{\mathrm{c}}(s)$$
$$+ \big[\boldsymbol{k}_1 + \boldsymbol{k}_2\boldsymbol{G}_{22}(s) + \boldsymbol{k}_3\boldsymbol{G}_{32}(s) + \boldsymbol{k}_{\mathrm{I}}/s\big]\boldsymbol{i}_{\mathrm{c}}(s)\Big\}$$
(19)

where the transfer functions from $\boldsymbol{u}_{\mathrm{c}}$ to $\hat{\boldsymbol{u}}_{\mathrm{f}}$ and from $\boldsymbol{i}_{\mathrm{c}}$ to $\hat{\boldsymbol{u}}_{\mathrm{f}}$ are

$$\boldsymbol{G}_{21}(s) = \frac{\hat{\boldsymbol{u}}_{\mathrm{f}}(s)}{\boldsymbol{u}_{\mathrm{c}}(s)} = \mathbf{C}_{\mathrm{u}}(s\mathbf{I} - \mathbf{A} + \mathbf{L}\mathbf{C}_{\mathrm{c}})^{-1}\mathbf{B}_{\mathrm{c}}$$

$$\boldsymbol{G}_{22}(s) = \frac{\hat{\boldsymbol{u}}_{\mathrm{f}}(s)}{\boldsymbol{i}_{\mathrm{c}}(s)} = \mathbf{C}_{\mathrm{u}}(s\mathbf{I} - \mathbf{A} + \mathbf{L}\mathbf{C}_{\mathrm{c}})^{-1}\mathbf{L},$$

respectively. The transfer functions $\boldsymbol{G}_{31}(s) = \hat{\boldsymbol{i}}_{\mathrm{g}}(s)/\boldsymbol{u}_{\mathrm{c}}(s)$ and $\boldsymbol{G}_{32}(s) = \hat{\boldsymbol{i}}_{\mathrm{g}}(s)/\boldsymbol{i}_{\mathrm{c}}(s)$ are obtained from (12) in a similar way. Using relationships (2), (14), and (19), the loop-transfer function is

$$\boldsymbol{H}(s) = \Big\{\boldsymbol{k}_1\boldsymbol{Y}(s) + \boldsymbol{k}_2[\boldsymbol{G}_{21}(s) + \boldsymbol{Y}(s)\boldsymbol{G}_{22}(s)]$$
$$+ \boldsymbol{k}_3[\boldsymbol{G}_{31}(s) + \boldsymbol{Y}(s)\boldsymbol{G}_{32}(s)] + (\boldsymbol{k}_{\mathrm{I}}/s)\boldsymbol{Y}(s)\Big\} \quad (20)$$
$$\cdot G_{\mathrm{d}}(s)G_{\mathrm{L}}(s).$$

The poles of $\boldsymbol{H}(s)$ are the union of the poles of the separate transfer functions of (20). Further, there are no right half-plane poles in $\boldsymbol{Y}(s)$ and the poles of the observer transfer functions and the phase-lead compensator can be freely selected to be in the left half-plane. According to the Nyquist stability criterion, if there are no right half-plane poles in $\boldsymbol{H}(s)$ and the Nyquist plot of $\boldsymbol{H}(s)$ does not encircle the point of $-1+\mathrm{j}0$, the system is stable [25].

Let us examine the Nyquist stability criterion in an example case. A sketch of the Nyquist diagram of the loop-transfer function is shown in Fig. 3 when ω_{g} is set to zero for simplicity. In this case, due to the integrator and the dynamics of the LCL filter (2), there are two poles at $s = 0$ turning the phase of the plot $-360°$ clockwise when the gain is infinity. This path is further marked with the symbols $0-$ and $0+$. At the resonance frequency, the phase is turning $-180°$ clockwise, i.e., to the negative direction as in Fig. 2, and the gain is infinity (due to the omitted losses) resulting another large arc at infinity. This path is further marked with the symbols $\omega+$. There is a similar path at the negative frequencies, marked with $\omega-$, which is symmetric in this example (but asymmetric if $\omega_{\mathrm{g}} \neq 0$). If $\omega_{\mathrm{g}} \neq 0$, the arcs at infinities remain similar at the resonance frequencies; only the arc of $s = 0$ is splitted into two parts, another originating from the imaginary pole $s = -\mathrm{j}\omega_{\mathrm{g}}$.

Fig. 3.   Nyquist diagram of the loop-transfer function $\boldsymbol{H}(s)$. The grid frequency ω_{g} is set to zero to give a simple presentation of the controlled system. Note, that the symmetry of the diagram is lost when $\omega_{\mathrm{g}} \neq 0$.

As can be seen from Fig. 3, the Nyquist plot does not encircle the critical point of $-1 + \mathrm{j}0$. The system is stable. Furthermore, there is a small modulus margin M (or vector margin), which is the distance to the critical point from the closest approach of the plot. The modulus margin is suitable for analyzing complex systems in which the magnitude and phase may cross 1 and $-180°$, respectively, several times [25], [26].

The loop-transfer function $\boldsymbol{H}(s)$ and Nyquist diagrams provide a tool for examining stability with varying parameters and parameter errors. For example, in the case of a varying grid inductance, the controller gains are calculated with nominal parameters, given in Table I, and a parameter error ΔL_{fg} is taken into account in the sub-transfer functions of (20). The real inductance in the circuit is $L_{\mathrm{fg}} + \Delta L_{\mathrm{fg}}$. For example, applying relative errors $\Delta L_{\mathrm{fg}}/L_{\mathrm{fg}} = -0.3$, $\Delta L_{\mathrm{fg}}/L_{\mathrm{fg}} = 0$ and $\Delta L_{\mathrm{fg}}/L_{\mathrm{fg}} = 0.3$, the Nyquist diagrams of $\boldsymbol{H}(s)$ are presented in Fig. 4 with the controller, observer, and phase-lead compensator parameters given in Table II.

The controller is tuned by setting the natural frequency $\omega_1 = 2\pi \cdot 500$ rad/s of the dominant dynamics (corresponding to the approximate bandwidth of $f_{\mathrm{sw}}/12 = 500$ Hz). The resonance frequency $\omega_2 = \omega_{\mathrm{p}}$ is damped by selecting $\zeta_2 = 0.1$ in order to ensure stability in the worst-case scenario with the selected bandwidth and parameter uncertainty of 30%. It is to be noted that the damping ratio ζ_2 is limited by the delay T_{d} in the control system. If the delay is zero, the damping ratio could be selected almost arbitrarily within the limits of the control effort, but with a delay of $T_{\mathrm{d}} = 3T_{\mathrm{s}}/2$, the selection of ζ_2 is limited to lower values (depending on the selected dominant dynamics, resonance frequency, and phase-lead compensation). As an example, if the delay were

TABLE I
SYSTEM PARAMETERS

Param.	Value	Param.	Value
u_g	$\sqrt{2/3} \cdot 400$ V (1 p.u.)	ω_g	$2\pi \cdot 50$ rad/s
i_N	$\sqrt{2} \cdot 18$ A (1 p.u.)		
L_{fc}	2.94 mH (0.072 p.u.)	L_{fg}	1.96 mH (0.048 p.u.)
C_f	10 μF (0.040 p.u.)	u_d	650 V (2 p.u.)
ω_p^s	$2\pi \cdot 1470$ rad/s	ω_z^s	$2\pi \cdot 1140$ rad/s
f_{sw}	6 kHz	T_s	$1/(2f_{sw})$

TABLE II
STATE-SPACE CONTROLLER PARAMETERS

Param.	Value	Param.	Value
ω_1	$2\pi \cdot 500$ rad/s	ζ_1	0.9
ω_2	$\omega_p = \omega_p^s - \omega_g$	ζ_2	0.1
α_{o1}	$2\omega_1$		
ω_{o2}	ω_p	ζ_{o2}	0.5
ϕ_m	13.8°	A_L	$1/k_L$, cf. (18)

decreased by increasing the switching frequency to $f_{sw} = 10$ kHz, the phase-lead compensator would not needed and a higher damping ratio of $\zeta_2 = 0.3$ could be selected. These limitations can be examined by means of Nyquist diagrams. Lower values of the damping ratio will cause some oscillations in the worst-case scenario, but with the losses of a real LCL filter, effective damping is sufficient.

The dominant dynamics of the observer are selected to be twice as fast as the control bandwidth. The resonant dynamics of the observer are set at the resonance frequency. Based on the delay analysis, $\mathrm{PM_R} = 26.2°$ according to (15). The phase lead of $\phi_m = 13.8°$ is used to produce the phase margin of 40° at the resonance frequency ω_p with the unity controller. However, the bandwidth, damping ratio, and phase lead could be selected differently, since control tuning is a compromise between dynamic performance and robustness. The analysis based on the Nyquist diagrams enables optimization of the damping ratio and phase-lead compensation, if the design specifications and system parameters are known.

The Nyquist plots of Fig. 4 do not encircle the critical point, i.e., the system is stable with the selected controller tuning and the relative parameter errors of $\Delta L_{fg}/L_{fg} = -0.3$, $\Delta L_{fg}/L_{fg} = 0$, and $\Delta L_{fg}/L_{fg} = 0.3$. If the parameter error of the filter capacitor C_f is considered instead, the system is stable with the equivalent errors of $\Delta C_f/C_f = -0.3$, $\Delta C_f/C_f = 0$, and $\Delta C_f/C_f = 0.3$. By means of a similar analysis, it can be shown that a more robust system could be achieved at the expense of dynamic performance: the system becomes less sensitive to the parameter errors, if the natural frequency ω_1 of the dominant dynamics is lowered.

F. Practical Implementation

Practical implementation issues are discussed in this subsection. Regarding to the integrator of the state-space controller, the anti-windup is implemented by feeding back the difference of the possibly saturated output $\mathrm{sat}(\boldsymbol{u}_c)$ and the control voltage, as described for PI control in [27]. Then, the reference value of the current for the integral part of the controller is
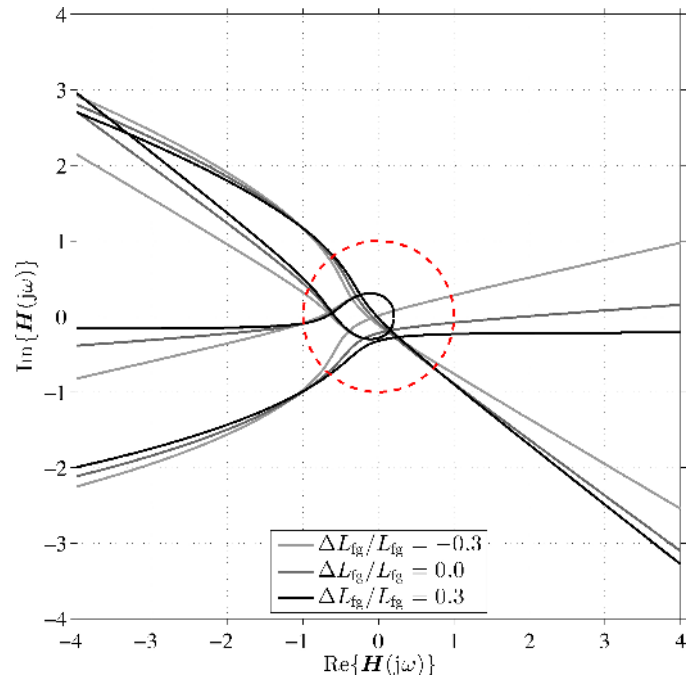
Fig. 4.   Nyquist diagrams of the loop-transfer function $\boldsymbol{H}(s)$ when the inductance L_{fg} is varying. The real inductance in the circuit is $L_{fg} + \Delta L_{fg}$.

limited

$$\tilde{\boldsymbol{i}}_{c,ref} = \boldsymbol{i}_{c,ref} + \boldsymbol{k}_T^{-1}[\mathrm{sat}(\boldsymbol{u}_c) - \boldsymbol{u}_{c,ref}]. \tag{21}$$

Actually, PI control can be seen as a special case of state-space control given in (5). With the selections

$$\boldsymbol{k}_1 = k_p + R_a - j\omega_g L_{fc} \tag{22a}$$

$$\boldsymbol{k}_2 = \boldsymbol{k}_3 = 0 \tag{22b}$$

$$\boldsymbol{k}_T = k_p \tag{22c}$$

$$\boldsymbol{k}_I = k_i \tag{22d}$$

the state-space controller is equivalent to a two-degree-of-freedom (2DOF) PI controller in [9] with the gains k_p and k_i, the active damping term R_a, and the approximate cross-coupling compensation $j\omega_g L_{fc}$.

For implementation of the proposed method, the control system is discretized using Tustin's bilinear equivalent [25]

$$s = \frac{2}{T_s}\frac{1 - z^{-1}}{1 + z^{-1}}. \tag{23}$$

In the case of the phase-lead compensator, the discrete algorithm is obtained inserting (23) in (16). For a general state-space presentation, i.e., $\mathrm{d}\mathbf{x}'/\mathrm{d}t = \mathbf{A}'\mathbf{x}' + \mathbf{B}'\mathbf{u}'$ and $\mathbf{y}' = \mathbf{C}'\mathbf{x}' + \mathbf{D}'\mathbf{u}'$, Tustin's method can be written as [28]:

$$\mathbf{w}(k+1) = \mathbf{\Phi}\mathbf{w}(k) + \mathbf{\Gamma}\mathbf{u}'(k) \tag{24a}$$

$$\mathbf{y}'(k) = \mathbf{C}_d\mathbf{w}(k) + \mathbf{D}_d\mathbf{u}'(k) \tag{24b}$$

where $\mathbf{w}$ is the modified state vector and the discretized system

matrices are

$$\boldsymbol{\Phi} = (\mathbf{I} + T_\mathrm{s}/2 \cdot \mathbf{A}')(\mathbf{I} - T_\mathrm{s}/2 \cdot \mathbf{A}')^{-1} \qquad (25a)$$

$$\boldsymbol{\Gamma} = \sqrt{T_\mathrm{s}}(\mathbf{I} - T_\mathrm{s}/2 \cdot \mathbf{A}')^{-1}\mathbf{B}' \qquad (25b)$$

$$\mathbf{C}_\mathrm{d} = \sqrt{T_\mathrm{s}}\mathbf{C}'(\mathbf{I} - T_\mathrm{s}/2 \cdot \mathbf{A}')^{-1} \qquad (25c)$$

$$\mathbf{D}_\mathrm{d} = \mathbf{D}' + T_\mathrm{s}/2 \cdot \mathbf{C}'(\mathbf{I} - T_\mathrm{s}/2 \cdot \mathbf{A}')^{-1}\mathbf{B}' \qquad (25d)$$

In the state-space controller, only the integrator needs to be discretized using (24) and (25), i.e., $\mathbf{y}' = \mathbf{x}' = \boldsymbol{x}_\mathrm{I}$, $\mathbf{u}' = \tilde{\boldsymbol{i}}_{\mathrm{c,ref}} - \boldsymbol{i}_\mathrm{c}$, $\mathbf{A}' = 0$, $\mathbf{B}' = 1$, $\mathbf{C}' = 1$, and $\mathbf{D}' = 0$, leading to a fairly simple algorithm. In the case of the state observer, the gain vector $\mathbf{L}$ is packed into system matrices and the matrices and vectors for the discretization are: $\mathbf{y}' = \mathbf{x}' = \hat{\mathbf{x}}$, $\mathbf{u}' = [\boldsymbol{u}_\mathrm{c} \; \boldsymbol{u}_\mathrm{g} \; \boldsymbol{i}_\mathrm{c}]^\mathrm{T}$, $\mathbf{A}' = \mathbf{A} - \mathbf{L}\mathbf{C}_\mathrm{c}$, $\mathbf{B}' = [\mathbf{B}_\mathrm{c} \; \mathbf{B}_\mathrm{g} \; \mathbf{L}]$, $\mathbf{C}' = \mathbf{I}$, and $\mathbf{D}' = 0$.

IV. SIMULATION AND EXPERIMENTAL RESULTS

Simulations and experiments were used to verify the proposed current control method. An experimental setup consists of two back-to-back connected 12.5-kVA 50-Hz converters equipped with LCL filters, an isolation transformer for the loading converter, and dSPACE DS1006, DS2201, and DS5202 boards with associate hardware for the control algorithms, PWM, and analog measurements of the converter under test. The system parameters are given in Table I. The converter under test was controlling the DC-bus voltage, while another converter was used to feed the load to the bus. The switching frequency was $f_\mathrm{sw} = 6$ kHz (unless otherwise noted).

In the simulations, the load was a constant current source and the grid was considered to be stiff. The frequency-dependent losses of real inductors are considerable in the vicinity of the resonance frequency [29]. In the simulation model, the LCL filter was built using a first-order series Foster model for the inductors [29], [30]: 102-mΩ and 68-mΩ resistors are used in series with L_fc and L_fg, respectively; and 420-Ω and 630-Ω resistors are used in parallel with L_fc and L_fg, respectively. The series resistances are based on the measured DC resistance of the filter. The parallel resistances were selected to match the simulated losses with the measured losses of the filter at the nominal power.

A. Validation

First, the simulation results are compared with the experimental results in order to validate the simulation model. The example design, whose parameter sensitivity was analyzed in Section III-F, is considered. The step of 10 A (0.4 p.u.) in the reference $i_{\mathrm{cq,ref}}$ of the converter current was applied. The reference $i_{\mathrm{cd,ref}}$ was determined by the active power transfer through the DC-voltage control. No active power, except the losses of the setup, was transferred in this test. The responses of the converter-current components and grid-current components are shown in Figs. 5 and 6, respectively. The time scale of 20 ms used in the figures equals one period of the 50-Hz grid voltage.

As can be seen from the results, the simulated and measured dominant dynamics match the designed dynamics: the current
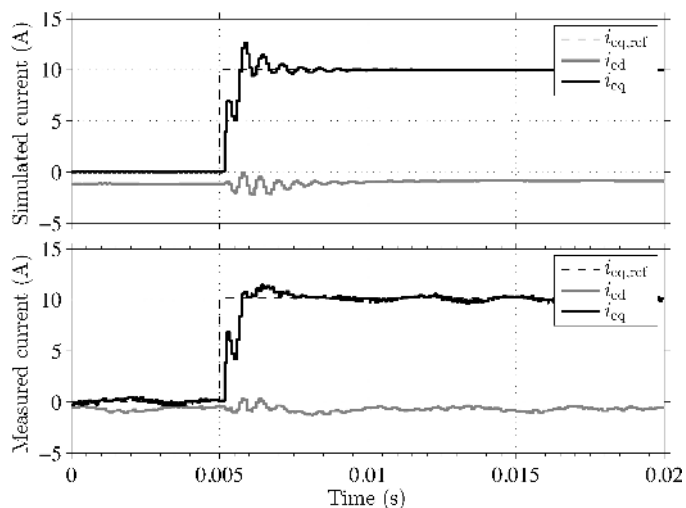
Fig. 5.   Simulated (above) and measured (below) step responses of the converter current components i_{cd} and i_{cq}.
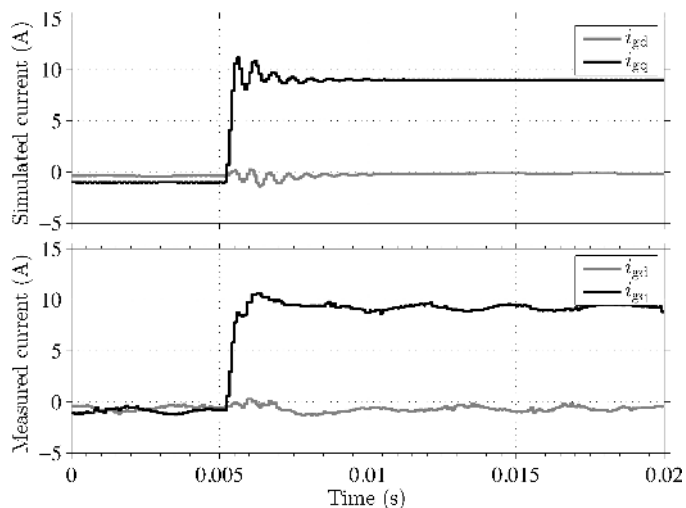
Fig. 6.   Simulated (above) and measured (below) step responses of the grid current components i_{gd} and i_{gq}.
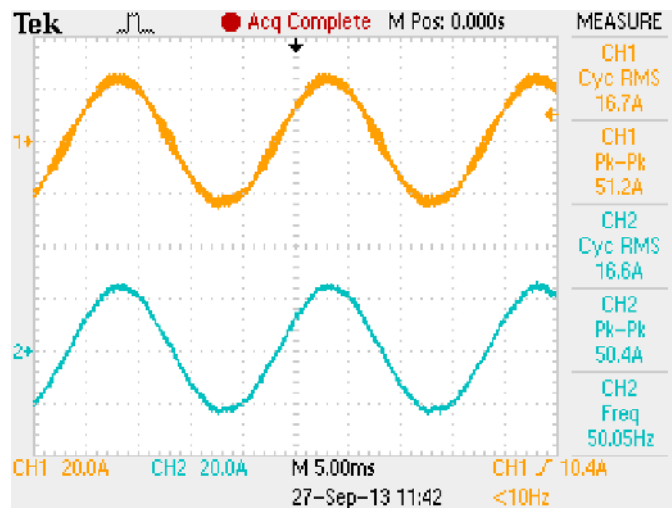
Fig. 7.   Converter-side phase current i_{ca} (above) and the grid-side phase current i_{ga} (below). The converter operates slightly below the nominal point.
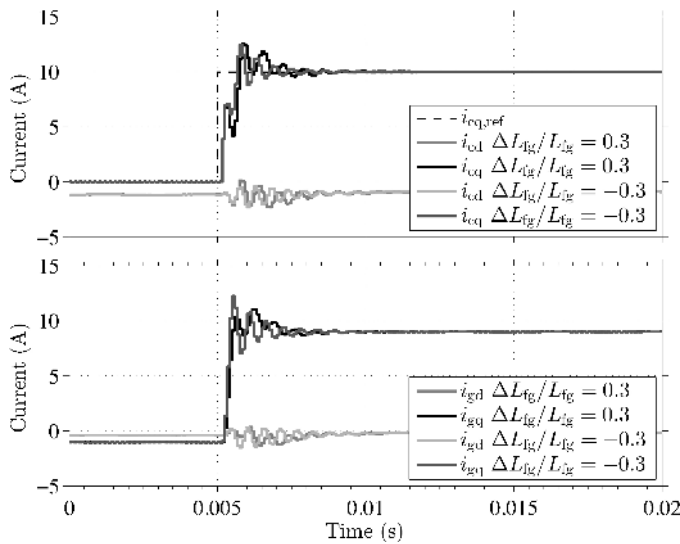
Fig. 8.   Simulated converter and grid current step responses with parameter errors $\Delta L_{\mathrm{fg}}/L_{\mathrm{fg}} = -0.3$ and $\Delta L_{\mathrm{fg}}/L_{\mathrm{fg}} = 0.3$.
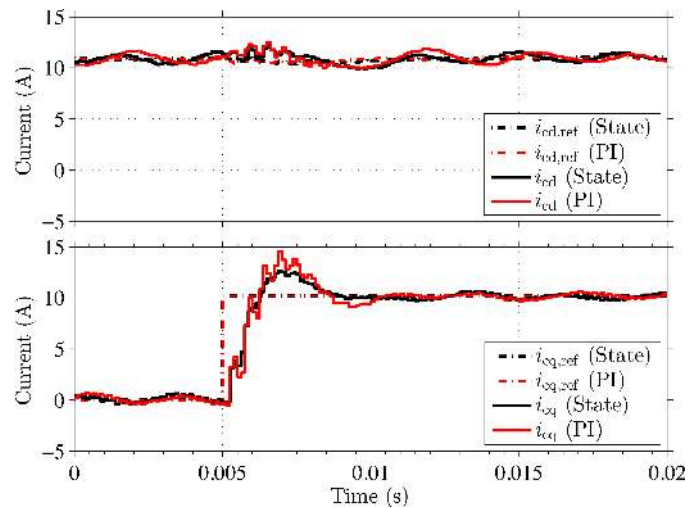

Fig. 9.   Comparison of state-space and PI control. Measured responses of the converter current components i_{cd} and i_{cq}. For both control methods under comparison, the switching frequency was decreased to $f_{\mathrm{sw}} = 4$ kHz.
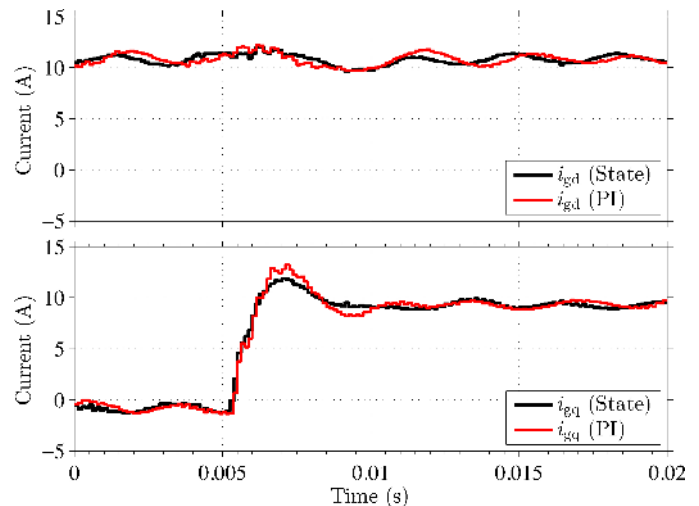

Fig. 10.   Comparison of state-space and PI control. Measured responses of the grid current components i_{gd} and i_{gq}. For both control methods under comparison, the switching frequency was decreased to $f_{\mathrm{sw}} = 4$ kHz.

rises to its reference in 0.75 ms. The cross-coupling between the d and q components is well compensated. The minor cross-coupling oscillations at the resonance frequency originate from the time delay. In the resonant dynamics, simulations show slightly more oscillations in comparison with the experimental results. This is because of the simple model of the LCL filter was used in the simulations. In order to model high-frequency behavior of the inductors more accurately, the order of the Foster model could be increased [29], [30].

The proposed method is also validated when the converter is supplying the nominal power. Fig. 7 shows the measured converter-side and grid-side phase currents. Total harmonic distortions (THD) up to the 50th harmonic of the converter and grid currents are 2.6% and 2.9%, respectively.

B. Parameter Errors

In Section III-F, the effect of the varying grid inductance was examined with the Nyquist diagrams. The corresponding cases of the parameter errors $\Delta L_{\mathrm{fg}}/L_{\mathrm{fg}} = -0.3$ and $\Delta L_{\mathrm{fg}}/L_{\mathrm{fg}} = 0.3$ were simulated and the results are shown in Fig. 8. The results are in line with the analysis, cf. Fig 4. The system remains stable with the parameter variation and the resonance behavior is close to the nominal situation shown in Figs. 5 and 6. Only the resonance frequency is changing due to the change in the actual inductance $L_{\mathrm{fg}} + \Delta L_{\mathrm{fg}}$, i.e., the larger inductance decreases the resonance frequency.

C. Comparison With 2DOF PI Control

The proposed state-space current controller was compared with a 2DOF PI controller, cf. (22), where the controller gains were $k_{\mathrm{p}} = \alpha_{\mathrm{c}} L_{\mathrm{fc}}$, $k_{\mathrm{i}} = \alpha_{\mathrm{c}}^2 L_{\mathrm{fc}}$, and $R_{\mathrm{a}} = \alpha_{\mathrm{c}} L_{\mathrm{fc}}$ [9]. The tuning parameter α_{c} was selected so that the rise time equals that in the proposed method.

For both control methods under comparison, the switching frequency was decreased to $f_{\mathrm{sw}} = 4$ kHz in order to demonstrate the smaller ratio of the delay frequency $\omega_{\mathrm{d}} = 2\pi/T_{\mathrm{d}}$

to the resonance frequency ω_{p}. The other system parameters equal the values given in Table I. The delay frequency $\omega_{\mathrm{d}} < 4\omega_{\mathrm{p}}$, leading to the negative phase margin of $\mathrm{PM_R} = -5.7°$ according to (15). To compensate the delay, the phase lead of $\phi_{\mathrm{m}} = 35.7°$ was produced at the resonance frequency, corresponding to the target phase margin of $30°$ with the unity controller. The other parameters of the state-space controller were kept the same as in Table II. For a fair comparison, the same phase-lead compensator was used with the both control methods under comparison. It is important to note that, when the switching frequency is 4 kHz, the system is unstable with the both controllers if no phase lead is used.

Figures 9 and 10 show the measured converter and grid currents when a step of 10 A (0.4 p.u.) in the reference $i_{\mathrm{cq,ref}}$ was applied at $t = 5$ ms. Approximately the power of 5 kW (0.4 p.u.) was transferred through the test setup, leading to $i_{\mathrm{cd}} \approx 10$ A. It can be seen that the resonance of the filter is

poorly damped in the case of the 2DOF PI controller. On the other hand, damping is sufficient in the case of the proposed state-space controller. Furthermore, the effect of the phase-lead compensator, having the gain $A_{\mathrm{L}} = 1/k_{\mathrm{L}}$, can be seen as slightly slower dominant dynamics in comparison with the results with $f_{\mathrm{sw}} = 6$ kHz. The amount of the phase lead could be decreased, which brings A_{L} closer to unity. Then, the dominant dynamics would be closer to the desired dynamics $\omega_1 = 2\pi \cdot 500$ rad/s.

V. Discussion

The proposed controller was analytically tuned by assuming the lossless LCL filter, which represents the worst-case scenario from the point of view of the filter resonance. With higher power ratings, reaching MVA ratings, the system losses are relatively smaller than those in the power ratings of a few kVA. Furthermore, the switching frequencies tend to be lower. In this paper, the simulation and experimental results were shown for a low-power converter. However, the proposed design approach can also be applied in the case of higher power ratings (if the same converter topology is used); this applicability was verified with simulations and analyses of Nyquist diagrams using the converter system parameters given in [1], [6], [18].

The proposed method was designed using converter-current feedback in order to enable installation of the current sensors inside the converter and to make protection of the converter straightforward. Furthermore, if the grid-voltage sensors were eliminated by means of estimation [6], [8], [15], [17], the amount of sensors would be less and the LCL filter would be physically separated from the converter, enabling modular assembly of the converter system. Instead of using converter-current feedback, the state-space controller could be redesigned for grid-current feedback using the proposed design process and design tools. In the case of grid-current feedback, the reactive power can be more accurately (i.e., independently of the model parameters) controlled at the point of common coupling. If the ratio of the resonance frequency $\omega_{\mathrm{p}}^{\mathrm{s}}$ to the sampling frequency $\omega_{\mathrm{s}} = 2\pi/T_{\mathrm{s}}$ is high ($\omega_{\mathrm{p}}^{\mathrm{s}}/\omega_{\mathrm{s}} > 1/6$), the system with grid-current feedback is easier to stabilize [4], [20], but then the previously mentioned advantages of converter-current feedback are lost.

The degrees of freedom in the control design are higher with the proposed state-space controller than those in the case of the 2DOF PI controller, leading to better dynamic performance and resonance damping. The proposed state observer increases complexity of the control algorithm in comparison with measurement of the states. However, contrary to the control methods in [5], [10], [13], the proposed method enables implementation of the state-space controller using the same amount of sensors as in the case of the 2DOF PI controller [9], some of the virtual resistor designs [7], capacitor-voltage feedback [1], [12], filtering output of the current controller [3], [4] and passive damping [2].

If the state-space controller were designed in the discrete-time domain [10], [11], [13], [14], [16], the discretization of the controller is not needed and dynamic performance might be slightly better, since the delay can be integrated in the system model. With predictive methods [17], [18], performance could be further improved. However, in the proposed scheme, simpler expressions for the gains are obtained and the connection between the physical parameters and control is retained at the same time. Furthermore, the cross-coupling is automatically compensated for through the proposed pole-placement method.

VI. Conclusion

This paper presented a continuous-time design method for an observer-based state-space current controller of a grid-connected converter equipped with an LCL filter. Model-based pole placement was used to derive an analytical design for a state-space controller and a full-order observer. The ratio of the resonance frequency to the delay frequency was examined, and a phase-lead compensator was proposed to compensate for the phase lag of the delay. The Nyquist stability criterion was used to examine the robustness of the proposed method against varying grid inductance. The method was verified with simulations and experiments; the results indicate more effective resonance damping of the LCL filter and better dynamic performance in comparison with a 2DOF PI controller. The proposed model-based design approach enables automatic tuning of the controller, if the parameters of the LCL filter are known or can be estimated. Furthermore, the proposed method gives a solid basis for our future research focusing on grid-voltage sensorless operation.

References

[1] V. Blasko and V. Kaura, "A novel control to actively damp resonance in input LC filter of a three-phase voltage source converter," *IEEE Trans. Ind. Appl.*, vol. 33, no. 2, pp. 542–550, Mar./Apr. 1997.

[2] M. Liserre, F. Blaabjerg, and S. Hansen, "Design and control of an LCL-filter-based three-phase active rectifier," *IEEE Trans. Ind. Appl.*, vol. 41, no. 5, pp. 1281–1291, Sep./Oct. 2005.

[3] M. Liserre, A. Dell'Aquila, and F. Blaabjerg, "Genetic algorithm-based design of the active damping for an LCL-filter three-phase active rectifier," *IEEE Trans. Power Electron.*, vol. 19, no. 1, pp. 76–86, Jan. 2004.

[4] J. Dannehl, M. Liserre, and F. W. Fuchs, "Filter-based active damping of voltage source converters with LCL filter," *IEEE Trans. Ind. Electron.*, vol. 58, no. 8, pp. 3623–3633, Aug. 2011.

[5] E. Twining and D. G. Holmes, "Grid current regulation of a three-phase voltage source inverter with an LCL input filter," *IEEE Trans. Power Electron.*, vol. 18, no. 3, pp. 888–895, May 2003.

[6] M. Malinowski and S. Bernet, "A simple voltage sensorless active damping scheme for three-phase PWM converters with an LCL filter," *IEEE Trans. Ind. Electron.*, vol. 55, no. 4, pp. 1876–1880, Apr. 2008.

[7] P. A. Dahono, "A control method to damp oscillation in the input LC filter," in *Conf. Proc. IEEE PESC 2002*, vol. 4, Cairns, Australia, 2002, pp. 1630–1635.

[8] W. Gullvik, L. Norum, and R. Nilsen, "Active damping of resonance oscillations in LCL-filters based on virtual flux and virtual resistor," in *Proc. Eur. Conf. on Power Electron. Appl. EPE 2007*, Aalborg, Denmark, Sep. 2007, pp. 1–10.

[9] L. Harnefors, L. Zhang, and M. Bongiorno, "Frequency-domain passivity-based current controller design," *IET Power Electronics*, vol. 1, no. 4, pp. 455–465, Dec. 2008.

[10] E. Wu and P. W. Lehn, "Digital current control of a voltage source converter with active damping of LCL resonance," *IEEE Trans. Power Electron.*, vol. 21, no. 5, pp. 1364–1373, Sep. 2006.

[11] C. Ramos, A. Martins, and A. Carvalho, "Complex state-space current controller for grid-connected converters with an LCL filter," in *Proc. IEEE IECON 2009*, Porto, Portugal, Nov. 2009, pp. 296–301.

[12] I. J. Gabe, V. F. Montagner, and H. Pinheiro, "Design and implementation of a robust current controller for VSI connected to the grid through an LCL filter," *IEEE Trans. Power Electron.*, vol. 24, no. 6, pp. 1444–1452, Jun. 2009.

[13] J. Dannehl, F. W. Fuchs, and P. B. Thøgersen, "PI state space current control of grid-connected PWM converters with LCL filters," *IEEE Trans. Power Electron.*, vol. 25, no. 9, pp. 2320–2330, Sep. 2010.

[14] M. Xue, Y. Zhang, Y. Kang, Y. Yi, S. Li, and F. Liu, "Full feedforward of grid voltage for discrete state feedback controlled grid-connected inverter with LCL filter," *IEEE Trans. Power Electron.*, vol. 27, no. 10, pp. 4234–4247, Oct. 2012.

[15] B. Bolsens, K. De Brabandere, J. Van den Keybus, J. Driesen, and R. Belmans, "Model-based generation of low distortion currents in grid-coupled PWM-inverters using an LCL output filter," *IEEE Trans. Power Electron.*, vol. 21, no. 4, pp. 1032–1040, Jul. 2006.

[16] F. Huerta, S. Cobreces, E. Bueno, F. Rodriguez, F. Espinosa, and C. Giron, "Control of voltage source converters with LCL filter using state-space techniques," in *Proc. of IEEE IECON 2008*, Orlando, FL, Nov. 2008, pp. 647–652.

[17] S. Mariéthoz and M. Morari, "Explicit model-predictive control of a PWM inverter with an LCL filter," *IEEE Trans. Ind. Electron.*, vol. 56, no. 2, pp. 389–399, 2009.

[18] V. Miskovic, V. Blasko, T. Jahns, A. Smith, and C. Romenesko, "Observer based active damping of LCL resonance in grid connected voltage source converters," in *Proc. IEEE ECCE 2013*, Denver, CO, Sep. 2013, pp. 4850–4856.

[19] N. Hoffmann, M. Hempel, M. C. Harke, and F. W. Fuchs, "Observer-based grid voltage disturbance rejection for grid connected voltage source PWM converters with line side LCL filters," in *Proc. IEEE ECCE 2012*, Raleigh, NC, Sep. 2012, pp. 69–76.

[20] S. G. Parker, B. P. McGrath, and D. G. Holmes, "Regions of active damping control for LCL filters," in *Proc. IEEE ECCE 2012*, Raleigh, NC, Sep. 2012, pp. 53–60.

[21] J. Dannehl, C. Wessels, and F. W. Fuchs, "Limitations of voltage-oriented PI current control of grid-connected PWM rectifiers with LCL filters," *IEEE Trans. Ind. Electron.*, vol. 56, no. 2, pp. 380–388, Feb. 2009.

[22] S.-K. Chung, "A phase tracking system for three phase utility interface inverters," *IEEE Trans. Power Electron.*, vol. 15, no. 3, pp. 431–438, May 2000.

[23] L. Harnefors and H.-P. Nee, "A general algorithm for speed and position estimation of AC motors," *IEEE Trans. Ind. Electron.*, vol. 47, no. 1, pp. 77–83, Feb. 2000.

[24] R. I. Bojoi, G. Griva, V. Bostan, M. Guerriero, F. Farina, and F. Profumo, "Current control strategy for power conditioners using sinusoidal signal integrators in synchronous reference frame," *IEEE Trans. Power Electron.*, vol. 20, no. 6, pp. 1402–1412, Nov. 2005.

[25] G. F. Franklin, J. D. Powell, and A. Emami-Naeini, *Feedback Control of Dynamic Systems*.   New Jersey: Prentice-Hall, 2002.

[26] A. G. Yepes, F. D. Freijedo, O. Lopez, and J. Doval-Gandoy, "Analysis and design of resonant current controllers for voltage-source converters by means of nyquist diagrams and sensitivity function," *IEEE Trans. Ind. Electron.*, vol. 58, no. 11, pp. 5231–5250, Nov. 2011.

[27] Y. Peng, D. Vrancic, and R. Hanus, "Anti-windup, bumpless, and conditioned transfer techniques for PID controllers," *IEEE Control Syst. Mag.*, vol. 16, no. 4, pp. 48–57, Aug. 1996.

[28] G. F. Franklin, J. D. Powell, and M. Workman, *Digital Control of Dynamic Systems*.   Menlo Park, CA: Addison-Wesley, 1997.

[29] M. Routimo and H. Tuusa, "LCL type supply filter for active power filter — comparison of an active and a passive method for resonance damping," in *Proc. IEEE PESC 2007*, Orlando, FL, Jun. 2007, pp. 2939–2945.

[30] F. de Leon and A. Semlyen, "Time domain modeling of eddy current effects for transformer transients," *IEEE Trans. Power Del.*, vol. 8, no. 1, pp. 271–280, Jan. 1993.

Jarno Kukkola received the B.Sc. (Tech.) and M.Sc. (Tech.) degrees from Aalto University, Espoo, Finland, in 2010 and 2012, respectively.

Since 2010, he has been with the Aalto University. He is currently working towards the D.Sc. (Tech.) degree in the Aalto University School of Electrical Engineering, Espoo, Finland. His main research interest is grid-connected converters.

Marko Hinkkanen (M'06–SM'13) received the M.Sc.(Eng.) and D.Sc.(Tech.) degrees from Helsinki University of Technology, Espoo, Finland, in 2000 and 2004, respectively.

Since 2000, he has been with Helsinki University of Technology (part of Aalto University, Espoo, since 2010). He is currently an Assistant Professor with the Aalto University School of Electrical Engineering. His research interests include power-electronic converters, electric machines, and electric drives.